

LARGE-EDDY SIMULATION BASED STUDY OF OFFSHORE WIND TURBINE ARRAY BOUNDARY LAYERS

D. Yang¹, C. Meneveau¹, L. Shen^{2†}

¹Johns Hopkins University, Department of Mechanical Engineering,
Baltimore, MD 21218, USA, di_yang@jhu.edu, meneveau@jhu.edu

²University of Minnesota, Department of Mechanical Engineering and
St. Anthony Falls Laboratory, Minneapolis, MN 55455, USA, shen@umn.edu

ABSTRACT

A hybrid numerical model is developed for the simulation of offshore wind farms. In the model, the wind turbulence is simulated using the large-eddy simulation technique; the ocean wave field is simulated using a potential-flow based method; and the wind and wave simulations are coupled through a two-way feedback scheme. The effect of wind turbines on the wind field is represented by an actuator disk model. Using this numerical model, the effect of ocean waves on the wind farm dynamics is studied by considering a variety of fully-developed and fetch-limited wind-sea conditions. The simulation results indicate that the offshore wind farm obtains a higher wind power extraction rate under the fully-developed wind-sea condition compared with the fetch-limited condition.

INTRODUCTION

Having larger available space, higher wind energy, and relatively less visual impact and noise, offshore wind power has become a new frontier of wind energy study. Unlike their land-based counterparts, offshore wind farms are operated in a complex environment in which the sea surface is covered by progressive surface waves of various sizes that interact with the wind over a wide range of scales. Thus, better understanding of the offshore wind farm dynamics and accurate predictions of offshore wind farm performance require consideration of turbine–wind–wave coupling dynamics.

In recent years, advancements in large-eddy simulation (LES) of atmospheric flows combined with wind turbine models have made LES a useful tool for wind energy research (e.g., Jimenez *et al.* [1, 2]; Troldborg *et al.* [3]; and Wu and Porté-Agel [4]). By performing LES of a wind turbine array with periodic lateral boundary conditions, Calaf *et al.* [5] were able to capture the complex interaction of wind turbine wakes as well as the large-scale interaction between the wind farms and the atmospheric boundary layer. Particularly, their statistical analyses of the LES results revealed that for a fully developed wind turbine array boundary layer, the wind at

[†] Author to whom correspondence should be addressed.

the turbine rotor height obtains kinetic energy mainly through the vertical flux of energy from the atmosphere above, rather than from horizontal energy flux.

While wind power on land is being actively explored, there is a lack of LES tools for the simulation of offshore wind farms. In this study, a hybrid numerical capability is developed for the simulation of large-scale offshore wind farms. The numerical framework consists of: (i) a LES of wind turbulence on a curvilinear coordinate that follows the wave surface motion [6]; (ii) a spectral simulation of nonlinear sea-surface waves with high resolution, which is dynamically coupled with the wind LES [7]; and (iii) an actuator-disk model for the wind turbines. For the first time, these modeling tools are coupled in the simulation to capture the complex flow physics of the offshore wind farms.

Following Calaf *et al.* [5], in our simulation, a very large wind farm is modeled with an “infinite” turbine array (by means of periodic boundary conditions in the horizontal directions). The turbine array boundary layer is considered to be fully developed. The sea surface is covered by wind-generated wave field, with both fetch-limited condition and fully-developed condition being considered. For the wind farm configuration, various streamwise spacing (i.e. $s_x = 10.5, 7, \text{ and } 5.25$, with s_x being the ratio of streamwise turbine spacing to the turbine diameter) are investigated. Based on the simulation data, the characteristics of offshore wind turbine array boundary layer are studied.

This paper is organized as follows. First, the numerical method used in our hybrid model is introduced, followed by the validation of the model. Next, the problem setup and the parameters for the simulation cases are discussed. The results of these cases are then analyzed to study the effect of ocean waves on wind farm dynamics. Finally, conclusions are given.

NUMERICAL METHOD

For the wind field, we consider a neutrally stratified atmospheric boundary layer flow in a horizontally periodic domain. The coordinate system is denoted as $x_i (i = 1, 2, 3) = (x, y, z)$, where x and y are the horizontal coordinates and z is the vertical coordinate, with $z = 0$ being the mean sea surface. The velocity components in x -, y -, and z -directions are denoted as $u_i (i = 1, 2, 3) = (u, v, w)$, respectively.

In LES, the motion of wind turbulence is described by the filtered Navier–Stokes equations for incompressible flows,

$$\frac{\partial \tilde{u}_i}{\partial t} + \tilde{u}_j \frac{\partial \tilde{u}_i}{\partial x_j} = -\frac{1}{\rho_a} \frac{\partial \tilde{p}^*}{\partial x_i} - \frac{\partial \tau_{ij}^d}{\partial x_j} - \frac{1}{\rho} \frac{\partial p_\infty}{\partial x} \delta_{i1} + f_T \delta_{i1}, \quad (1)$$

$$\frac{\partial \tilde{u}_i}{\partial x_i} = 0. \quad (2)$$

Here, $(\tilde{\dots})$ indicates filtering at the grid scale Δ ; ρ_a is the density of air; $\tau_{ij} = \widetilde{u_i u_j} - \tilde{u}_i \tilde{u}_j$ is the subgrid-scale (SGS) stress tensor, and τ_{ij}^d is its trace-free part; and $\tilde{p}^* = \tilde{p} + \tau_{kk}/3 - p_\infty$ is the filtered modified pressure. In this study, we consider the condition of mean wind being perpendicular to the wind turbine rotor plane, i.e. along the $+x$ -direction. The imposed pressure gradient $\partial p_\infty / \partial x$ models the effect of geostrophic wind forcing [5]. The friction velocity for the

wind above the turbine array is thus $u_* = \sqrt{-\overline{H}(\partial p_\infty/\partial x)/\rho_a}$, where \overline{H} is the height of the top boundary of the simulation domain with respect to the mean sea surface.

In this study, we consider the sea surface being covered by pure wind-generated waves. Under such conditions, the floating offshore wind turbine platforms from many of the practical designs, e.g., the MIT/NREL TLP [8] and the WindFloat [9], result in only small motions in response to the wind and waves. Therefore, in this study, we neglect the motions of the platform and assume the wind turbines to be fixed in space. The turbine-induced force in Eq. (1), f_T , is calculated by the actuator-disk model originally applied in LES by Jimenez *et al.* [1, 2]. In the present study, we use the modified version proposed by Meyers and Meneveau [10]. In this model, the turbine induced force per unit mass in the streamwise direction is given by

$$f_T(x_i, y_j, z_k) = -\frac{1}{2} \frac{C_T}{(1-a)^2} \langle u^T \rangle_d^2 \frac{\gamma_{j,k}}{\Delta x}. \quad (3)$$

Here, (x_i, y_j, z_k) denotes the position of a given grid point with index (i, j, k) ; $C_T = 3/4$ is the thrust coefficient and $a = 1/4$ is the induction factor [1, 5]; $\langle u^T \rangle_d$ is the local reference wind velocity evaluated by spatial averaging over all grid points within the turbine disk; $\gamma_{j,k}$ is the fraction of area overlap between the grid cell (j, k) and the turbine rotor circle; and Δx is the streamwise grid size.

In Eq. (1), the SGS stress tensor is modeled using the Lagrangian-averaged scale-dependent dynamic Smagorinsky model, as described in Bou-Zeid *et al.* [11]. On the other hand, the molecular viscous term is neglected because the Reynolds number for the flows considered in this study is very high. This also prevents the resolving of the turbulence boundary layer near the wave surface. Consequently, in the simulation, a surface-layer model is employed to impose proper sea-surface stress to the wind turbulence, which is expressed as [11]

$$\tau_{i3}^{SGS}(x, y, t) = - \left[\frac{\kappa}{\ln(d_2/z_0)} \right]^2 \widehat{U}_r(x, y, t) \widehat{u}_{r,i}(x, y, t), \quad i = 1, 2. \quad (4)$$

Here, $\kappa = 0.4$ is the von Kármán constant; $(\widehat{\dots})$ indicates filtering at the test-filter scale 2Δ ; z_0 is the sea-surface roughness associated with the SGS waves; $\widehat{u}_{r,i}$ are the filtered horizontal wind velocities relative to the water surface at the first off-surface grid-point (i.e., in the LES code, at height d_2 above the sea surface),

$$\widehat{u}_{r,i}(x, y, t) = \widehat{u}_i(x, y, d_2, t) - \widehat{u}_{s,i}(x, y, t), \quad i = 1, 2. \quad (5)$$

Here, the values of $\widehat{u}_{s,i}$ are obtained by the test-filtering of the sea surface velocities $u_{s,i}$; and

$$\widehat{U}_r(x, y, t) = \sqrt{\left[\widehat{u}_r(x, y, t) \right]^2 + \left[\widehat{v}_r(x, y, t) \right]^2} \quad (6)$$

is the magnitude of horizontal wind velocity relative to the wave surface.

In the simulations, the streamwise and spanwise boundaries are treated as periodic, so that the finite number of wind turbines in the simulation domain represent a subset of an infinitely large wind farm [5]. The top of the simulation domain is considered to be rigid and slip-free.

The bottom is bounded by the wave surface, with von Neumann condition for the velocity field given by Eq. (4). A time-dependent boundary-fitted grid is used to follow the curvature of the wave surface. The irregular wave surface-bounded domain in the physical space is transformed to a right rectangular prism in the computational space using an algebraic mapping [6].

For spatial discretization, we use a Fourier-series-based pseudo-spectral method on a collocated grid in the horizontal directions, and a second-order finite-difference method on a staggered grid in the vertical direction. The governing equations are integrated in time with a fractional-step method. First, the momentum equations without the pressure terms are advanced in time with a second-order Adams–Bashforth scheme. Then, a Poisson equation is solved for the pressure to provide correction for the velocity field so that the incompressibility constraint is satisfied. The effect of resolved-scale sea-surface waves on the wind field, i.e. the form drag, is captured by this wave-correlated pressure field. The details and validations of the numerical scheme are provided in Yang and Shen [6].

The motion of the sea-surface waves is simulated using a high-order spectral method (HOSM) [12]. The HOSM simulates nonlinear waves using the Zakharov formulation [13], in which the wave motion is described by the surface elevation η and the surface potential Φ^s . Here, $\Phi^s = \Phi(x, y, z = \eta(x, y, t), t)$ with Φ being the velocity potential. With a perturbation series of Φ with respect to the wave steepness to the order of M and Taylor series expansion about the mean water level $z = 0$,

$$\Phi^s(x, y, t) = \sum_{m=1}^M \sum_{\ell=0}^{M-m} \frac{\eta^\ell}{\ell!} \frac{\partial^\ell}{\partial z^\ell} \Phi^{(m)}(x, y, z, t) \Big|_{z=0}, \quad (7)$$

and an eigenfunction expansion of each $\Phi^{(m)}$ with N modes,

$$\Phi^{(m)}(x, y, z, t) = \sum_{k=1}^N \Phi_k^{(m)}(t) \Psi_k(x, y, z), \quad (8)$$

the kinematic and dynamic free surface boundary conditions are written as [12]

$$\frac{\partial \eta}{\partial t} = -\nabla_h \eta \cdot \nabla_h \Phi^s + (1 + |\nabla_h \eta|^2) \left[\sum_{m=1}^M \sum_{\ell=0}^{M-m} \frac{\eta^\ell}{\ell!} \sum_{k=1}^N \Phi_k^{(m)} \frac{\partial^{\ell+1} \Psi_k}{\partial z^{\ell+1}} \Big|_{z=0} \right], \quad (9)$$

$$\frac{\partial \Phi^s}{\partial t} = -g\eta - \frac{|\nabla_h \Phi^s|^2}{2} - \frac{p_a(x, y, t)}{\rho_w} + \frac{1 + |\nabla_h \eta|^2}{2} \left[\sum_{m=1}^M \sum_{\ell=0}^{M-m} \frac{\eta^\ell}{\ell!} \sum_{k=1}^N \Phi_k^{(m)} \frac{\partial^{\ell+1} \Psi_k}{\partial z^{\ell+1}} \Big|_{z=0} \right]^2. \quad (10)$$

In this paper, we consider deep water waves, for which the eigenfunctions Ψ_k are

$$\Psi_k(x, y, z) = \exp(|\mathbf{k}|z + \mathbf{i}\mathbf{k} \cdot \mathbf{x}). \quad (11)$$

Here $\mathbf{i} = \sqrt{-1}$; and $\mathbf{k} = (k_x, k_y)$ is the wavenumber vector, which is related to the scalar wavenumber k through $k = |\mathbf{k}| = \sqrt{k_x^2 + k_y^2}$. In HOSM, Eqs. (9) and (10) are advanced in time by a fourth-order Runge–Kutta scheme. The equations are discretized in space by a Fourier-series-based pseudo-spectral method. The quadratic terms are de-aliased with the 3/2 rule. The HOSM simulation of sea-surface wave field is coupled with the LES of wind turbulence through a

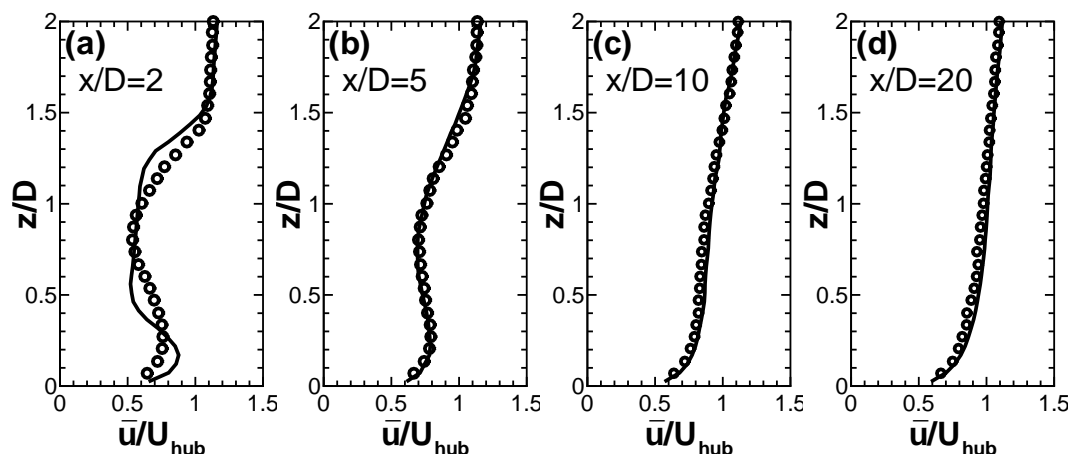


Figure 1: Vertical profiles of time-averaged velocity \bar{u} at the central cross-section of the wake behind a single turbine at four downstream locations: (a) $x/D = 2$; (b) $x/D = 5$; (c) $x/D = 10$; and (d) $x/D = 20$. Here, D is the diameter of the turbine rotor, and U_{hub} is the mean inflow wind velocity measured at $1D$ upstream of wind turbine hub. The wind tunnel measurement data of Chamorro and Porté-Agel [16] is denoted by \circ , and the current LES result is denoted by — .

fractional-step scheme. Details and validations of the coupling scheme are given in Yang and Shen [7].

VALIDATION

The current turbulence flow solver has been tested extensively for various wind–wave problems [14, 15, 6, 7]. Therefore, the validation of wind–wave interaction simulation is not taken up in this paper. Here, we focus on the validation of wind turbine modeling by comparing the current LES result with existing experimental data in the literature.

We perform a LES of air flow past a single wind turbine, with the parameters matching those in the laboratory measurement of Chamorro and Porté-Agel [16]. The wind turbine has a diameter of $D = 0.15$ m and a hub height of $H_{\text{hub}} = 0.125$ m. The mean inflow velocity (measured at $1D$ upstream of wind turbine hub) is $U_{\text{hub}} = 2.2$ m/s. The wind friction velocity is $u_* = 0.102$ m/s. The bottom boundary is flat and has a surface roughness of 0.03 mm. The simulation domain has a size of $(L_x, L_y, \bar{H}) = (4.32, 0.72, 0.46)$ m. The domain is sufficiently long in the streamwise direction ($L_x/D = 28.8$), so that the effect of periodic boundary condition on the statistics of the inflow wind towards the turbine rotor is negligibly small. The grid resolution is $N_x \times N_y \times N_z = 256 \times 48 \times 64$, with evenly distributed grid points in all of the three directions.

Figure 1 shows the vertical profiles of time-averaged streamwise velocity \bar{u} at the central cross-section of the turbine wake. LES results at $x/D = 2, 5, 10$, and 20 are shown. The wind-tunnel measurement data from Chamorro and Porté-Agel [16] are plotted for comparison. Using an actuator-disk model of the wind turbine, the current LES captures the velocity deficit in the wake behind the turbine rotor ($0.33 < z/D < 1.33$, with the center of turbine rotor at $z/D =$

Table 1: Parameters of wave spectra for the HOSM simulations. Here, U_{10} is the mean wind velocity at the height of 10m above the mean water level; and F is the distance over which the wind has been blowing the water surface. At the peak of the wave spectra (denoted by the subscript ‘ p ’), k_p is the wavenumber; and c_p is the wave phase speed.

wave spectrum	U_{10} (m/s)	F (km)	k_p (m^{-1})	c_p (m/s)
JONSWAP	12.5	80.0	0.1	9.7
P–M	12.5	∞	0.04	15.3

$H_{\text{hub}}/D = 0.83$). The magnitude of velocity deficit obtained by the current LES agrees with the measurement data. In the near-turbine region (figure 1a), the LES result shows a relatively flat velocity profile within the turbine rotor region. This flattening is caused by the use of the disk-averaged reference velocity in the actuator-disk model when calculating the turbine-induced force (Eq. 3). Similar LES results have also been reported by Wu and Porté-Agel [4]. At the further downstream locations (Fig. 1b), the mean wind velocity profiles obtained by the LES agrees very well with the wind-tunnel measurement data. Due to the turbulent mixing, the mean velocity at hub height recovers and increases to $0.70U_{\text{hub}}$ at $x/D = 5$, compared with $0.56U_{\text{hub}}$ at $x/D = 2$.

PROBLEM SETUP

For the simulation of offshore wind farms, we consider a turbulent wind turbine array boundary layer over an open sea area. For the sea-surface wave field, we consider both fetch-limited and fully-developed sea conditions. For a wind-sea with limited fetch (defined as the distance of waves being blown by wind, and denoted by F), we use the wave spectrum obtained during the Joint North Sea Wave Observation Project (JONSWAP) [17]. For a fully developed sea, its surface wave field satisfies the Pierson–Moskowitz (P–M) spectrum [18]. In this study, we consider an environmental wind field (before encountering the wind farm) with a mean wind velocity of $U_{10} = 12.5$ m/s at the height of 10m above the mean water level. The key parameters of the corresponding wave fields for the given wind condition are listed in Table 1.

For the LES of offshore wind farms, we consider an $N_{\text{row}} \times 3$ wind turbine array within the simulation domain, which is a periodic representation of a large wind farm under fully developed condition. Here, N_{row} is the number of turbine rows (in the streamwise direction) in the simulation domain, and three values of $N_{\text{row}} = 2, 3$, and 4 are considered in this study. For these three values of N_{row} , the cases for JONSWAP wave condition are named as J2, J3, and J4, respectively; the cases for P–M wave condition are named as PM2, PM3, and PM4, respectively. The wind turbines have a hub height of $H_{\text{hub}} = 100$ m and a rotor diameter of $D = 100$ m. The computational domain of the LES has a size of $(L_x, L_y, \bar{H}) = (2.1, 1.5, 1.0)$ km, so that the streamwise wind turbine spacing parameter is $s_x = (L_x/N_{\text{row}})/D = 10.5, 7.0$, and 5.25 for $N_{\text{row}} = 2, 3$, and 4, respectively; and the spanwise spacing parameter has a fixed value of $s_y = (L_y/3)/D = 5.0$. The bottom of the wind field is bounded by sea-surface waves and has a prescribed value of 2.0×10^{-4} m for the subgrid-scale sea-surface roughness z_0 , consistent with typical observed values [19, 20].

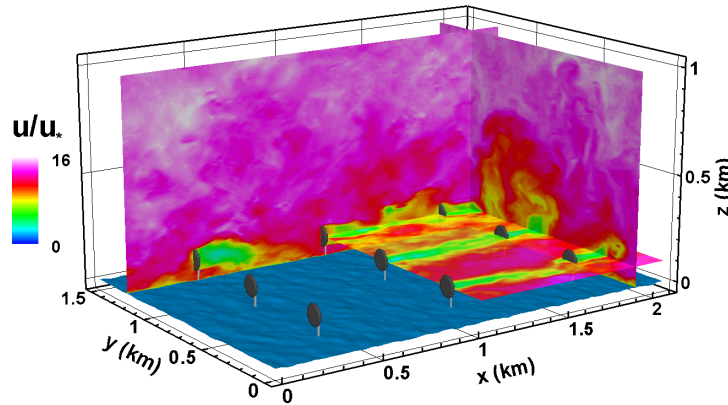


Figure 2: Illustration of three-dimensional flow field in the fully developed wind turbine array boundary layer over water waves for case PM3. Contours of instantaneous streamwise velocity u (normalized by u_*) are plotted on the three representative (x,y) -, (x,z) -, and (y,z) -planes. For the visualization of sea-surface waves, only half of the (x,y) -plane is shown.

For the LES, we use a grid resolution of $N_x \times N_y \times N_z = 192 \times 128 \times 192$, with evenly spaced grid in all of the three directions. For the HOSM, a higher horizontal grid resolution of $N_x \times N_y = 512 \times 384$ is used to resolve the energy-containing wave modes in the spectra. During the early stage of each simulation, the imposed pressure gradient Π in Eq. (1) is fine-tuned to approach a steady-state constant value so that the mean velocity at the top boundary U_{top} remains the same constant value among different cases. As a result, the wind turbine array boundary layer satisfies the desired geostrophic wind condition [5]. An example of the results of case PM3 is shown in Fig. 2.

We note that after the dynamically coupled wind and waves encounter the offshore wind farm, the wind speed near the sea surface is reduced and the waves near the spectrum peak propagate a bit faster than the wind. Therefore, within the wind farm region, the sea-surface wave field is effectively in a “fully developed” condition for both JONSWAP and P–M cases [18]. Under such condition, the wave field is able to maintain its basic spectral form without significant growth or decay. Thus the horizontally periodic boundary condition for both the wind farm and the wave field serves as a reasonable assumption in the current LES.

RESULTS

For wind blowing over waves, the total streamwise stress acting on the wind at the sea surface consists of two components, i.e.

$$\tau_{\text{total}} = \underbrace{-\frac{\rho}{A} \iint_A \tau_{xz}^{\text{SGS}} dx dy}_{\tau_s} + \underbrace{\frac{1}{A} \iint_A \tilde{p}_s \frac{\partial \tilde{\eta}}{\partial x} dx dy}_{\tau_p}. \quad (12)$$

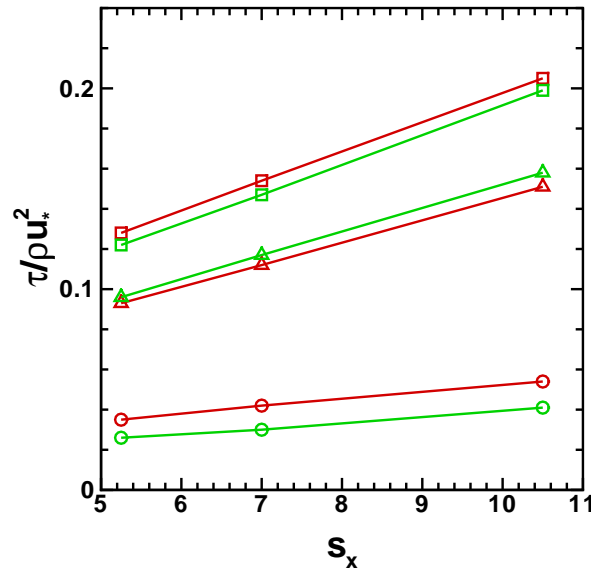


Figure 3: Budget of sea-surface stress as a function of streamwise turbine spacing s_x : Δ , surface shear stress τ_s ; \circ , wave form drag τ_p ; and \square , total surface stress τ_{total} . Results for JONSWAP wave condition are denoted by red color; results for P–M wave condition are denoted by green color.

Here, τ_s is the surface shear stress, with τ_{xz}^{SGS} given by Eq. (4); τ_p is the wave form drag, with \tilde{p}_s being the air pressure acting on the wave surface; and A is the total horizontal sea-surface area in the simulation domain.

Figure 3 shows the sea-surface stress budget for the various LES cases (represented as a function of s_x). Compared with the corresponding P–M wave cases, the JONSWAP wave cases have slightly smaller shear stress but larger wave form drag and total surface stress. Note that the dominant waves in the P–M cases are longer than those in the JONSWAP cases. Based on the dispersion relation of water waves, the dominant waves in the P–M cases are faster. Faster waves have smaller relative velocity with respect to the wind above. As a result, P–M cases have less wave form drag than JONSWAP cases. The current LES result is consistent with the results of previous studies on wind–wave interaction, which showed that faster waves induce smaller resistance to the wind [21]. Moreover, for a given wave condition, the turbine number per unit surface area increases as the streamwise turbine spacing s_x decreases. This results in an increase of turbine-induced stress and consequently a decrease of total surface stress τ_{total} (when normalized by the external wind friction velocity u_* above the turbine layer).

For the study of offshore wind farm dynamics, a key quantity to investigate is the power extraction rate of the wind farm. Based on the LES results, the power extracted by the wind turbines can be calculated directly based on the turbine induced force and wind velocity. Following

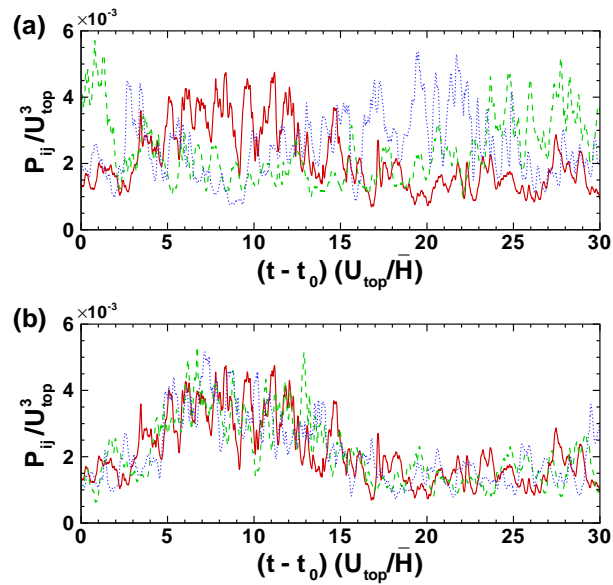


Figure 4: Extracted wind power density for wind turbines at different columns (denoted by ‘*c*’) and rows (denoted by ‘*r*’) for case J3. In (a), the three wind turbines in the first row are shown: red solid line, (*c*1, *r*1); green dashed line, (*c*2, *r*1); and blue dotted line, (*c*3, *r*1). In (b), the three wind turbines in the first column are shown: red solid line, (*c*1, *r*1); green dashed line, (*c*1, *r*2); and blue dotted line, (*c*1, *r*3). Here, U_{top} is the mean wind velocity at the top of the simulation domain; and t_0 is the time when statistical sampling starts.

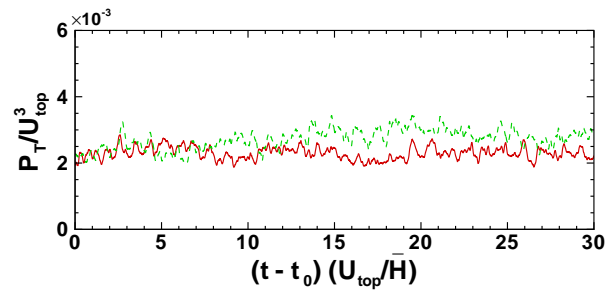


Figure 5: Averaged extracted power density of the wind farm for two different wave conditions: red solid line, J3; and green dashed line, PM3. Here, U_{top} is the mean wind velocity at the top of the simulation domain; and t_0 is the time that statistical sampling starts.

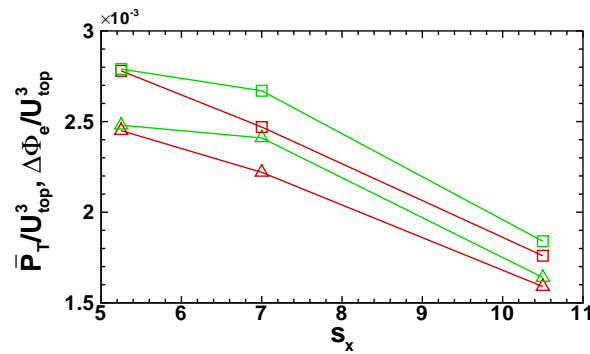


Figure 6: Time-averaged extracted power density of the wind farm and vertical flux of kinetic energy into the wind farm: Δ , \bar{P}_T ; and \square , $\Delta\Phi_e$. Results for JONSWAP wave condition are denoted by red color; results for P–M wave condition are denoted by green color.

Calaf *et al.* [5], the extracted power density by an individual wind turbine is defined as [5]

$$P_{ij} = \frac{\left(\frac{1}{2}C_T \frac{\pi}{4} D^2 \langle u^T \rangle_d^3\right)_{ij}}{s_x s_y D^2}, \quad (13)$$

where the subscript ‘ ij ’ denotes the turbine at the i -th row and j -th column. The averaged extracted wind power density over the entire wind farm is then calculated as

$$P_T = \frac{1}{N_{row} N_{col}} \sum_{i=1}^{N_{row}} \sum_{j=1}^{N_{col}} P_{ij}. \quad (14)$$

As illustrated in Fig. 2, there exists large spatial variation for the instantaneous wind field around different wind turbines, caused by the complex interactions among the turbines within the turbine array as well as their interactions with the atmospheric boundary layer. Consequently, the extracted power densities P_{ij} by different turbines exhibit appreciable variation, as shown in Fig. 4. Particularly, the variation of P_{ij} among turbines in different columns is significant in both long and short terms (Fig. 4a); the variation of P_{ij} among turbines in different rows is mainly in short term, and the long term variation is relatively small (Fig. 4b). Figure 5 shows the averaged power extraction rate P_T of the entire wind farm for cases J3 and PM3. The averaged performance of the entire wind farm has much less temporal variation than those of the individual turbines shown in Fig. 4.

The time-averaged values of P_T for various cases are calculated and plotted in Fig. 6. For a given turbine spacing, a wind farm above P–M waves extracts more power than that above JONSWAP waves. This increase of wind farm performance is caused by the stronger wave motion in the P–M wave cases compared with the JONSWAP wave cases. In the wake region behind each wind turbine, the strong deficit of wind speed causes waves to feed momentum back to wind. As shown in Table 1, under the same wind forcing, the fully-developed (P–M) wave field has larger peak wave phase speed than the fetch-limited (JONSWAP) wave field. As a result, within the turbine wake regions, the P–M waves have relatively stronger capability to help

recover the wind speed; out of the wake regions, the wind field experiences less wave resistance in the P–M wave cases than in the corresponding JONSWAP wave cases, resulting in slightly larger wind velocity near the wave surface as well as at the turbine rotor height. The turbines above the P–M waves thus have larger incident wind energy and achieve higher performance than the turbines above the JONSWAP waves.

When the streamwise turbine spacing decreases from $s_x = 10.5$ to $s_x = 7$, the near-surface wind velocity decreases and the long waves in the wave field become faster relative to the wind, resulting in an enhancement of the wave effect. Therefore, the difference of P_T between cases J3 and PM3 is larger than the difference between cases J2 and PM2. As the turbine spacing further decreases to $s_x = 5.25$, the distance between turbines is too small so that the waves in neither the P–M nor the JONSWAP cases have sufficient time to help recover the wind speed deficit in the turbine wake regions, thus resulting in insignificant difference between cases J4 and PM4.

Calaf *et al.* [5] showed that a large wind farm gains energy supplement mainly by the vertical flux of kinetic energy from the wind above it. The net kinetic energy flux into the wind farm can be calculated by

$$\Delta\Phi_e = \left[(-\langle \overline{u'w'} \rangle - \langle \overline{u''w''} \rangle) \langle \overline{u} \rangle \right]_{z=H_{\text{hub}}+D/2}^{z=H_{\text{hub}}-D/2}. \quad (15)$$

Here, the overbar \overline{u}_i denotes the time averaging; the brackets $\langle u_i \rangle$ denotes the horizontal averaging; $u'_i = u_i - \overline{u}_i$ denotes the fluctuating velocity due to temporal variation; and $u''_i = u_i - \langle \overline{u}_i \rangle$ denotes the fluctuating velocity due to both temporal and spatial variations. The values of $\Delta\Phi_e$ for various cases are also plotted in Fig. 6, which show consistent trend as \overline{P}_T when s_x changes. For all the cases, the values of \overline{P}_T and $\Delta\Phi_e$ are close, indicating the balance between the vertical energy flux and the turbine power extraction. The difference among them is caused mainly by kinetic energy dissipation through turbulence.

CONCLUSIONS

Offshore wind energy has become an important frontier of sustainable energy research. In this study, LES of wind turbulence coupled with potential flow simulation of ocean waves is performed for offshore wind farms. LES of the lower atmospheric boundary layer over ocean waves is performed using a boundary-fitted grid that follows the wave motion. The nonlinear evolution of the wave field is simulated using a high-order spectral method. Large wind farms are modeled as periodic wind turbine arrays, with the effect of turbines on the wind modeled using an actuator disc method. Statistical analysis of the wind farm dynamics shows that the wind field is influenced by the sea-surface waves due to the effect of wave-induced form drag. As a result, the energy extraction rate of the wind turbines varies with wave condition, with a higher extraction rate being obtained over fully-developed wind-sea conditions than over fetch-limited, developing wind-sea conditions.

ACKNOWLEDGEMENT

DY and LS acknowledge the support of NSF-CBET-1133700 and ONR-N00014-09-1-0395. CM acknowledges the support of NSF-AGS-1045189 and NSF-OISE-1243482.

REFERENCES

- [1] A. Jimenez, A. Crespo, E. Migoya, and J. Garcia, "Advances in large-eddy simulation of a wind turbine wake," *Journal of Physics: Conference Series* **75**, 012041 (2007).
- [2] A. Jimenez, A. Crespo, E. Migoya, and J. Garcia, "Large-eddy simulation of spectral coherence in a wind turbine wake," *Environmental Research Letters* **3**, 015004 (2008).
- [3] N. Troldborg, J. N. Sorensen, and R. Mikkelsen, "Numerical simulations of wake characteristics of a wind turbine in uniform inflow," *Wind Energy* **13**, 86 (2010).
- [4] Y.-T. Wu and F. Porté-Agel, "Large-eddy simulation of wind-turbine wakes: evaluation of turbine parametrisations," *Boundary-Layer Meteorol.* **138**, 345 (2011).
- [5] M. Calaf, C. Meneveau, and J. Meyers, "Large eddy simulation study of fully developed wind-turbine array boundary layers," *Phys. Fluids* **22**, 015110 (2010).
- [6] D. Yang and L. Shen, "Simulation of viscous flows with undulatory boundaries. Part I: Basic solver," *J. Comput. Phys.* **230** 5488 (2011).
- [7] D. Yang and L. Shen, "Simulation of viscous flows with undulatory boundaries. Part II: Coupling with other solvers for two-fluid computations," *J. Comput. Phys.* **230** 5510 (2011).
- [8] E. N. Wayman, P. D. Sclavounos, S. Butterfield, J. Jonkman, and W. Musial, "Coupled dynamic modeling of floating wind turbine systems," *Proceedings of the offshore technology conference, Houston, Texas, 1–4 May 2006*.
- [9] D. Roddier, C. Cermelli, A. Aubault, and A. Weinstein, "WindFloat: A floating foundation for offshore wind turbines," *J. Renewable Sustainable Energy* **2**, 033104 (2010).
- [10] J. Meyers and C. Meneveau, "Large eddy simulation of large wind-turbine arrays in the atmospheric boundary layer," *Proceedings of the 48th AIAA Aerospace Sciences Meeting Including the New Horizons Forum and Aerospace Exposition, AIAA 2010–827* (2010).
- [11] E. Bou-Zeid, C. Meneveau, and M. Parlange, "A scale-dependent lagrangian dynamic model for large eddy simulation of complex turbulent flows," *Phys. Fluids* **17**, 025105 (2005).
- [12] D. G. Dommermuth and D. K. P. Yue, "A high-order spectral method for the study of nonlinear gravity waves," *J. Fluid Mech.* **184**, 267 (1987).
- [13] V. E. Zakharov, "Stability of periodic wave of finite amplitude on the surface of a deep fluid," *J. Appl. Mech. Tech. Phys.* **2** 190 (1968).
- [14] D. Yang and L. Shen, "Characteristics of coherent vortical structures in turbulent flows over progressive surface waves," *Phys. Fluids* **21** 125106 (2009).
- [15] D. Yang and L. Shen, "Direct-simulation-based study of turbulent flow over various wavy boundaries," *J. Fluid Mech.* **650** 131 (2010).
- [16] L. P. Chamorro and F. Porté-Agel, "Effects of thermal stability and incoming boundary-layer flow characteristics on wind-turbine wakes: a wind-tunnel study," *Boundary-Layer Meteorol.* **136**, 515 (2010).

- [17] K. Hasselmann, T. P. Barnett, E. Bouws, H. Carlson, D. E. Cartwright, K. Enke, J. A. Ewing, H. Gienapp, D. E. Hasselmann, P. Kruseman, A. Meerburg, P. Müller, D. J. Olbers, K. Richter, W. Sell, and H. Walden, "Measurements of wind-wave growth and swell decay during the Joint North Sea Wave Project (JONSWAP)," *Dtsch. Hydrogr. Z. Suppl.* **8**, N12 (1973).
- [18] W. J. Pierson and L. Moskowitz, "A proposed spectral form for fully developed wind seas based on the similarity theory of S. A. Kitaigorodskii," *J. Geophys. Res.* **69**, 5181 (1964).
- [19] P. P. Sullivan, J. E. Edson, T. Hristov, and J. C. McWilliams, "Large-eddy simulations and observations of atmospheric marine boundary layers above nonequilibrium surface waves," *J. Atmos. Sci.* **65**, 1225 (2008).
- [20] P. P. Sullivan and J. C. McWilliams, "Dynamics of winds and currents coupled to surface waves," *Annu. Rev. Fluid Mech.* **42**, 19 (2010).
- [21] S. E. Belcher and J. C. R. Hunt, "Turbulent flow over hills and waves," *Annu. Rev. Fluid Mech.* **30**, 507 (1998).